Materials Today Quantum 6 (2025) 100041

Contents lists available at ScienceDirect

Materials Today Quantum

journal homepage: www.elsevier.com/locate/mtquan

Spin interactions in decorated graphene nanoflakes with two localized spin-1/2 entities☆

Toshikaze Kariyado

Research Center for Materials Nanoarchitectonics, National Institute for Materials Science, 1-1 Namiki, Tsukuba, 305-0044, Ibaraki, Japan

ARTICLE INFO

Keywords:
Graphene, Nanoflake, Quantum spin, First-principles calculation

ABSTRACT

Magnetic properties of graphene nanoflakes with designed edge shapes are theoretically analyzed by means of the first-principles calculation. As a starting point, we take a nanoflake with decorated zigzag edges where no magnetism is expected. Then, it is shown that removal of one decoration unit induces a well-defined localized spin-1/2 state. When two decoration units are removed, there arise two localized spin-1/2 states. Notably, when two spins are aligned in the same edge, the spin–spin interaction is ferromagnetic, while when two spins are aligned in the opposite edges, the spin–spin interaction is antiferromagnetic. This suggests that decorated nanoflakes form a promising playground for nanoscale spin devices with tunable spin–spin interactions by designing edge shapes.

1. Introduction

Electron spin is a minimal unit as a quantum information carrier, and thus the impact of enabling fine manipulations of electron spin can be maximal [1–4]. It may lead to better quantum information processing, denser information storage, or low-loss devices as a result of quantum effects. As a stage to host electron spins, molecules are interesting because of their large variety. A molecule can host spin-1/2 as a whole due to a radical molecular orbital. Some molecules contain atoms with spins (such as transition metals) as subparts of the host molecule. When a molecule is large enough, there arises a possibility of hosting multiple localized spins scattered around different parts of the host molecule. We expect a variety of interactions between scattered local spins, and one interesting consequence would be to realize a molecular device [5–7].

In line with this thought, graphene nanoflakes, which are small fragments of graphene sheets but can also be regarded as big molecules, form an interesting playground. It is well known that magnetism is induced at zigzag edges of graphene [8–11], while a nanoflake can have short sections of zigzag edges at its perimeter, suggesting a rich variety of spin interactions depending on the shapes of nanoflakes [12–16]. Indeed, an idea of realizing logic gates by nanoflake shape designs has already been posted [17,18]. There, a nanoflake based logic gate is designed by assembling smaller flakes, where each of the smaller flakes is designed to host a single spin-1/2 state originating from the existence of zigzag edges. The assembled flake is then regarded as a network of spin-1/2 states, where each spin acts as an input or output terminal. In order to realize useful devices, it is essential to tune interactions between spins. A rough but useful rule is that two spins living on the same sublattice of the honeycomb lattice tend to have a ferromagnetic coupling, while those living on the opposite sublattices tend to have an antiferromagnetic coupling [19,20]. For instance, in graphene nanoribbons with two zigzag edges at the both sides, spins on the same edge tend to have a ferromagnetic coupling, while spins on the opposite edges tend to have an antiferromagnetic coupling, since the roles of the two sublattices are switched between two edges [8–10]. This tendency has been confirmed in an experiment [21]. (Precisely speaking, the antiferromagnetic coupling between the opposite edges was found for relatively thin nanoribbons, and beyond some width around 7 nm, it switches to the ferromagnetic coupling.)

To modify magnetic properties in finite size graphene, edge termination is important [22,23]. It has been known that proper edge decorations can kill the edge states, and so the magnetism [24,25]. For instance, decorated edges in Fig. 1(a) along the lateral direction are one typical example of edges without magnetism, though the shown edge is aligned in the zigzag direction. Note that the unit length along the lateral direction is tripled from the pristine zigzag case. Nonexistence of magnetism with the tripled unit cell superstructure can be explained by a simple resonant theoretic analysis [24]. Or, it can also be understood by the edge band structure of graphene. It is known that a nearly flat band appears for the (pristine) zigzag edge of graphene, and the flat

☆ This work was supported by JSPS KAKENHI Grant Number JP24K06968. The part of calculations in this study have been done using the Numerical Materials Simulator at NIMS, and the facilities of the Supercomputer Center, the Institute for Solid State Physics, the University of Tokyo.

E-mail address: kariyado.toshikaze@nims.go.jp.

https://doi.org/10.1016/j.mtquan.2025.100041
Received 10 February 2025; Received in revised form 9 April 2025; Accepted 22 April 2025
Available online 5 May 2025

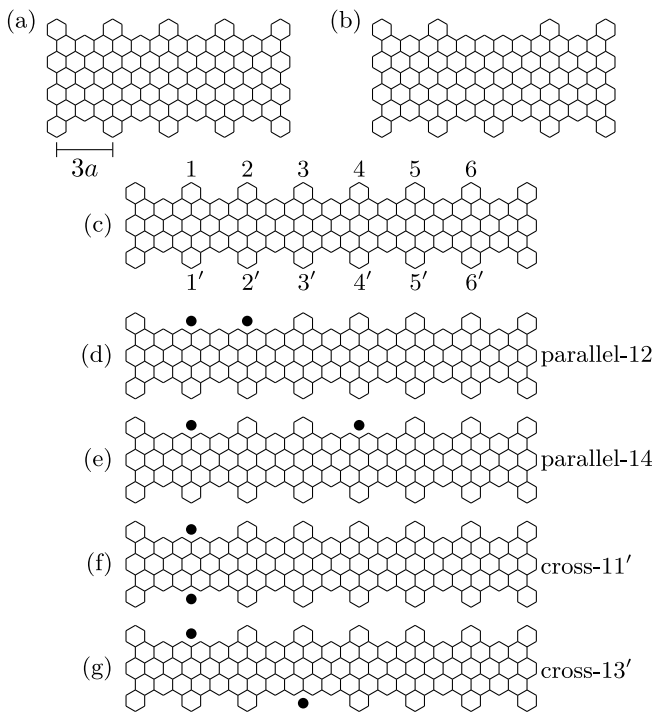

Fig. 1. Target structures of decorated nanoflakes. (a) Schematic picture of a nanoflake without port. a stands for the lattice constant of pristine graphene. (b) With a single port. (c) Definitions of port names in this paper for two port cases. (d–g) Nanoflakes with two ports. (d,e) For the case with two ports residing on the same edge (parallel types). (f,g) For the case with two ports residing on the opposite edges (cross types).

band covers 1/3 of the edge Brillouin zone [26], suggesting that the flat band can be gapped out to lose magnetism when a superstructure with tripled unit length is introduced. Interestingly, nanoribbons with the decoration pattern in Fig. 1(a) have already been fabricated in a bottom up way [27–29]. Another interesting aspect of the decoration in focus is that it plays an important role in manipulation of the topological edge states in the distorted honeycomb lattice model [30,31].

In this paper, we inspect spin–spin interactions in graphene nanoflakes whose shapes are derivatives of Fig. 1(a). As we have seen, no spins are expected at the upper and the lower edges in Fig. 1(a). Also, no spins are expected at the left and the right edges because the armchair type edge is known to host no magnetism. Then, an idea of introducing spins into this type of flakes is partially removing the decoration units at the lateral edges to recover short sections of pristine zigzag edges. Because one decoration unit per three times of the original unit length balances with the number of original edge states, removing one decoration unit leads to recovery of exactly one edge state, which potentially hosts a single spin-1/2 entity. For convenience, we name a removed part [i.e., the middle part at the upper edge in Fig. 1(b)] a *port* throughout the paper. In the following, we start with analysis of a flake in Fig. 1(b) as a typical example for single port cases to check that it really hosts a single spin-1/2 state. After that, we will move onto cases with two ports, aiming at deriving spin–spin interactions between two ports. There, we take a flake in Fig. 1(c) as a starting point. Note that the flake in Fig. 1(c) is longer than the one in Fig. 1(a) and (b), to see lateral distance dependence up to larger distance. Meanwhile, the width is reduced to ease the computational difficulty. In order to specify the target flake structure, we label the ports at the upper edge by 1 to 6, and the ports at the lower edge by $1'$ to $6'$ as in Fig. 1(c). Then, the target structure is specified by the labels of removed decoration units. For clarity, we also classify flakes with two ports by relative positioning of the two ports. Namely, when two ports are on the same edge, we call a flake *parallel* type, while when they are on the opposite sides, we call a flake *cross* type. Following these rules, the flakes in Fig. 1(d)–(g) are called parallel-12, parallel-14, cross-11′, and cross-13′, respectively. The names for the other possible structures can also be deduced straightforwardly.

2. Methods

To investigate structural, electronic, and magnetic properties of the target flakes, we employ the first-principles density functional theory (DFT) calculation using OpenMX package [32–35]. In OpenMX, the localized basis method, in particular, the pseudo-atomic orbital method is implemented. For the pseudo-atomic orbital method, what is critical for its accuracy is the number of basis orbitals for each atom. Predefined pseudo-atomic orbitals are provided by OpenMX package. Here, s2p1 and s2p2d1 type localized basis sets are used for H atoms and C atoms, respectively. In this naming notations, the letters s, p, and d represent angular dependence of the localized orbitals (i.e., the spherical harmonics) as usual, and integers associated with them represent numbers of radial functions for corresponding angular momentum sectors. Since s, p, and d orbitals contain 1, 3, and 5 harmonics, s2p1 means 5 (= 2+1×3) localized orbitals for H, and s2p2d1 means 13 (= $2\times1+2\times3+1\times5$) localized orbitals for C. We take PBE-GGA as an exchange–correlation functional [36]. Although the localized basis method is applied, integration over the space is required to calculate matrix elements for the Coulomb potential and the exchange–correlation potential, and plane waves with an energy cutoff of 350 Ry are used to represent charge density for the integration. In practice, "the space" is taken to be a $L_x\times L_y\times L_z$ cuboid box, where $(L_x, L_y, L_z) = (60, 50, 20)$ Å for the flake in Fig. 1(b), while $(L_x, L_y, L_z) = (75, 30, 20)$ Å for the flakes derived from Fig. 1(c), which have a large enough vacuum region around the flake. In the self-consistent field (SCF) cycles in DFT, the occupation of the Kohn–Sham orbitals are controlled by the Fermi distribution function with temperature 300 K. For the structural relaxation, the convergence criterion is such that the maximum remaining force goes below 1×10^{-4} Hartree/Bohr. For the electronic and magnetic structure analysis, we try both nonmagnetic and magnetic calculations, where for the magnetic case, spin polarized GGA is adapted. For the calculation with spins, the SCF cycles are started with C atoms residing in the ports being spin polarized to see whether the cycles flow into zero or finite localized spin moments. When there are two ports, we have two choices for the initial spin polarization of the C atoms in the ports, parallel or antiparallel, and we try both initial conditions to see the difference between ferromagnetic and antiferromagnetic couplings. Throughout the paper, perimeters of the flakes are always hydrogenated not to leave uncoupled σ-electrons in our analysis for stability.

3. Results – Single port

Let us start with the results for the single port case using the flake in Fig. 1(b). Fig. 2(a) shows the energy spectrum of the Kohn–Sham orbitals for the nonmagnetic calculation, where the energy is measured from the Fermi energy. The inset shows the relaxed structure (note that the hydrogenation at the edge is applied). There appears a clear gap of order 2 eV between (approximately) continuum valence and conduction spectra. This gap is originating from the confinement effect of the finite size flake, and inherited from the case without any ports. Throughout the paper, we call the gap between the valence continuum and the conduction continuum *the finite size gap* for consistency. The most important feature provided by the port is the in-gap state at the zero energy, whose wave function (not shown) is localized at the port. Theoretically, the key to understand the formation of the in-gap state is the imbalance between the total number of sublattices in the honeycomb structure. Focusing exclusively on the carbon π-electrons, and modeling the electronic states by a tight-binding model only with the nearest neighbor hoppings, it can be proven that if the number of two sublattices of the honeycomb lattice differs by $\Delta n_{\mathrm{sublat}}$ there should

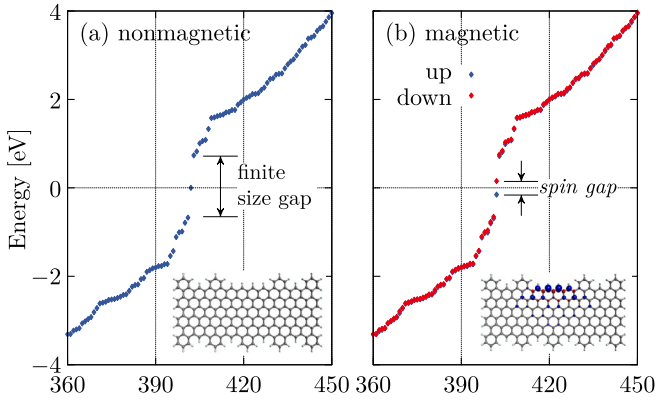

Fig. 2. Kohn–Sham energy spectra for (a) nonmagnetic and (b) magnetic cases. Horizontal axes show eigenstate index. Energies are measured from the Fermi energy. Insets show (a) the relaxed structure and (b) calculated spin density for the magnetic case. Note that the perimeter is hydrogenated. (For interpretation of the references to color in this figure legend, the reader is referred to the web version of this article.)

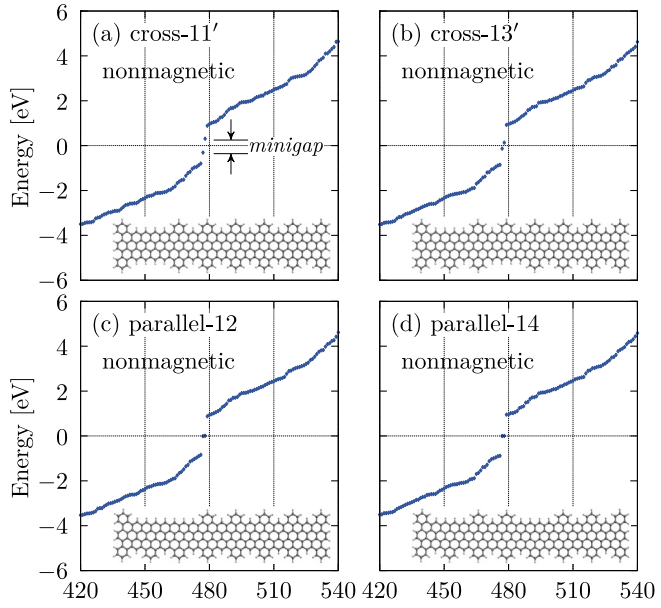

Fig. 3. Kohn–Sham energy spectra for several kinds of two port flakes, where horizontal axes show eigenstate index and energies are measured from the Fermi energy. Insets show corresponding relaxed structures. (a) to (d) correspond to cross-11′, cross-13′, parallel-12, and parallel-14, respectively.

arise $\Delta n_{\mathrm{sublat}}$ zero energy states [37]. A simple counting tells us that introducing one port results in $|\Delta n_{\mathrm{sublat}}| = 1$.

With the spin polarization turned on, the resultant energy spectrum of the Kohn–Sham orbitals is in Fig. 2(b), where the blue and the red dots are for the up spin states and the down spin states, respectively. The finite size gap is kept intact by the magnetic effects, while we see clear splitting of the in-gap zero energy state into a fully occupied up spin state and a fully empty down spin state, indicating the formation of the magnetic moment. For simplicity, we name this splitting *spin gap* in this paper. The inset of Fig. 2(b) shows the calculated spin density, confirming the localized nature of the induced magnetic moment. This proves our expectation that the removal of a single decoration unit results in a single localized spin-1/2 object.

4. Results – Two ports

Moving onto the two port cases, Fig. 3 shows the Kohn–Sham energy spectra obtained in the nonmagnetic calculations for the four selected

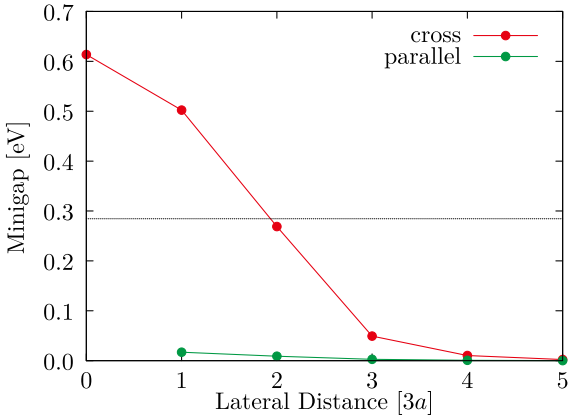

Fig. 4. Minigaps as functions of distance along the zigzag direction (lateral direction in the pictures for the structures) in the unit of $3a$, where a is the lattice constant of the pristine graphene. The red line for cross types and the green line for parallel types. The horizontal line in the middle shows the size of the spin gap for the single port case. Note that the lateral distance zero is not allowed for the parallel types. (For interpretation of the references to color in this figure legend, the reader is referred to the web version of this article.)

types, cross-11′, cross-13′, parallel-12, and parallel-14, respectively corresponding to Fig. 3(a)–(d). (The relaxed structures are shown as the insets.) We observe that the finite size gaps are nearly the same for the four cases. This supports a naive guess that the finite size gap depends only on the overall size of the flake, not on the port positions. On the other hand, it appears that the in-gap states are sensitive to the relative locations of the ports. Since we have two ports, two in-gap states are expected. For convenience, we name the gap between two in-gap states *minigap* throughout the paper. We see clear contrast between the cross types and the parallel types regarding the behavior of the minigaps. For the cross types [Fig. 3(a) and (b)], there appear sizable minigaps, and the minigap size depends on the lateral distance between the two ports, while for the parallel types [Fig. 3(a) and (b)] there are no significant minigaps irrespective of the lateral distance between the two ports. The difference can be accounted by $\Delta n_{\mathrm{sublab}}$ inspection. Since the roles of the sublattices are flipped at the upper edge and the lower edge, the cross types result in $\Delta n_{\mathrm{sublat}} = 0$, and nothing guarantees the formation of the zero modes, whilst the parallel types result in $|\Delta n_{\mathrm{sublat}}| = 2$, indicating a tendency to bind two states to zero energy. Tiny deviations from the zero energies are due to the minor effects such as influences from orbitals other than the carbon π-orbitals, or long range hoppings.

Fig. 4 shows the lateral distance dependence of the minigaps, where the red line is for the cross types and the green line is for the parallel types. For this calculation, one of the ports is fixed at position 1, meaning that the target flakes are in either cross-1μ' type or parallel-1μ type, where μ is a label integer. In order to have an insight for the formation of localized spins, the spin gap value for the single port case is indicated by a horizontal line in the middle (slightly below 0.3 eV). When the minigap exceeds the spin gap, naively, it is preferable to fill a state at the lower side of the minigap by up and down spin electrons, rather than to form a finite local spin moment. That is, when the minigap is larger than the spin gap, no local spin is expected and vice versa. Fig. 4 suggests that the cross types show a crossover between the state with localized spins and without localized spins as a function of the lateral distance between the two ports. On the other hand, we always expect the formation of localized spins for the parallel types.

Fig. 5 summarizes the total energies obtained in the magnetic calculations. As in Fig. 4, the horizontal axis is the lateral distance between the two ports. What we plot is the total energy difference between the magnetic case and the nonmagnetic case for each flake type, namely, the energy gain by the formation of the localized spin moment. As we have noted, two kinds of spin configurations are tested, antiferromagnetic (AFM) and ferromagnetic (FM). In Fig. 5, the solid

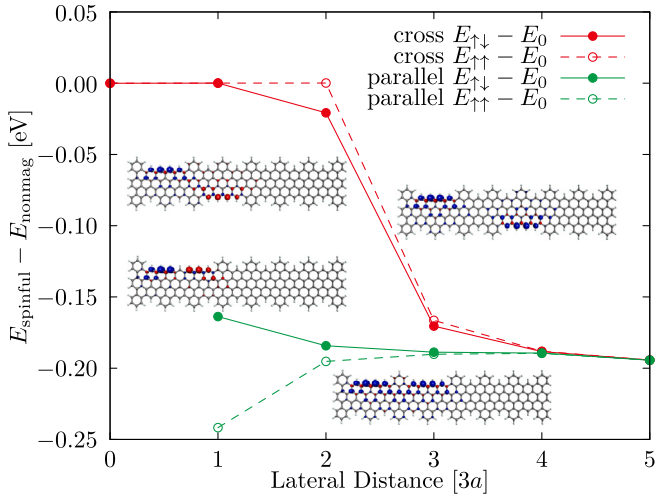

Fig. 5. Energy gain due to the formation of the localized magnetic moment. The red lines for the cross types and the green lines for the parallel types. The solid lines for antiferromagnetic spin configuration and the dashed line for the ferromagnetic spin configuration. Note that when the energy gain is zero, the local magnetic moment is calculated to be zero. (For interpretation of the references to color in this figure legend, the reader is referred to the web version of this article.)

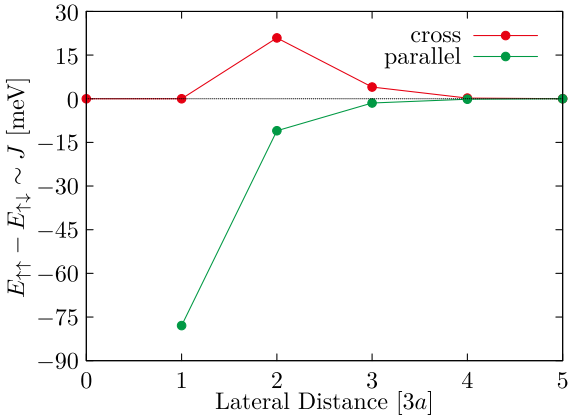

Fig. 6. Energy difference between the ferromagnetic and the antiferromagnetic spin configuration. (For interpretation of the references to color in this figure legend, the reader is referred to the web version of this article.)

and the dashed lines are for the AFM and the FM configurations, respectively, and the red and the green lines are for the cross and the parallel types. For the cross types, the energy gain sticks to zero in the small lateral distance for both of the AFM and FM cases, which is consistent with the dominance of the minigap effect. When the energy gain is zero, the SCF cycles of DFT automatically bring the local spin moment to zero, namely, the cycle flows into a nonmagnetic ground state. On the other hand, for the parallel types, the energy gain is always finite, i.e., always expecting the formation of a localized spin moment, which is consistent with the negligible minigap effect. The insets of Fig. 5 illustrate the calculated spin density for the selected cases with the finite energy gain, which clearly shows localization of spins as in the single port cases.

When the local spin moment arises, the AFM configurations are preferred (have lower energy) for the cross types, while the FM configurations are preferred for the parallel types. The FM states in the cross types and the AFM states in the parallel types appear as metastable states. This is consistent with the knowledge learned from the study of the zigzag nanoribbons: spin–spin interactions are FM along the ribbon while they are AFM across the ribbon. (Note that the width of the target flakes in this paper is about 1.5 nm, way less than 7 nm.) In the large lateral distance regime, the energy gains for the different types and the different spin configurations are merged. This is reasonable since when the two spins are separated by fairly large distances, the spin–spin interactions are expected to be small and the energy gains are accounted almost fully by the formation of the isolated localized spins, which is independent of the cross or the parallel types and the AFM or the FM configurations.

Then, let us estimate the spin–spin coupling constant from the data obtained so far. When there are two localized spin-1/2 entities, a minimal model Hamiltonian is

$$H = J\boldsymbol{S}_1 \cdot \boldsymbol{S}_2, \tag{1}$$

where $\boldsymbol{S}_i$ is the spin-1/2 operators. Within this treatment, the energy difference between the singlet state and the triplet state is J, with $J > 0$ corresponding to AFM coupling, while $J < 0$ corresponding to FM coupling. Although what we obtain in the DFT calculations are not exactly the spin singlet states and the triplet states, an estimation of J by the energy difference between the AFM state and the FM state is expected to be a reasonable approximation. The energy difference between the AFM and FM configurations are plotted as functions of the lateral distance in Fig. 6, where the red and green lines are for the cross and the parallel types, respectively. As it should be, the cross types give $J > 0$, while the parallel types give $J < 0$. For the small lateral distance, the cross types do not develop localized spins, and J values are meaningless for that cases, but we put zero values just as a reminder that the magnetism is killed. As the lateral distance becomes larger, $|J|$ decreases as expected from a naive intuition. The maximum $|J|$ reaches about 20 meV for the AFM coupling, and about 80 meV for the FM coupling.

5. Discussion and summary

The origin of the difference between the ferromagnetic and antiferromagnetic couplings can be accounted from the theorem in Ref. [37]. There, it is proven that for a repulsive Hubbard model (where the Coulomb interaction is described by onsite repulsion) on a bipartite lattice, the total spin of the ground state is $|\Delta_{\rm sublat}|/2$. Under the assumption that graphene is modeled by nearest neighbor hoppings between π-orbitals on a honeycomb lattice and short-range Coulomb repulsion between electrons, the theorem in Ref. [37] is applicable. Then, for the cross types with $\Delta n_{\rm sublat} = 0$, an antiferromagnetic coupling is expected between two localized spins to have zero net spin, while for the parallel types with $\Delta n_{\rm sublat} = 2$, a ferromagnetic coupling is expected between two localized spins to have a spin-1 ground state. Of course, the assumption regarding the nearest neighbor hoppings and onsite Coulomb repulsion is not strictly applied, and we need to confirm this idea by more realistic calculations as has been done in this manuscript.

To summarize, it is shown that the properly decorated nanoflakes form an excellent stage for tunable spin–spin interactions. The ferromagnetic and antiferromagnetic couplings can be switched by placing two ports at the same edge or the opposite edges, and the magnitude of the couplings can be tuned by changing the distance between the two ports. By investigating width dependence or different types of decorations, reachable parameter regime can be extended further. The proposed scheme is not only for molecular devices, but also for quantum simulators of one-dimensional quantum spin chains that have a long history of theoretical and experimental studies, by considering longer flakes or infinitely long nanoribbons. In this paper, we limit ourselves to collinear spin configurations, which is reasonable for two port cases. By introducing more than three ports, there may arise frustration. Or, by introducing the spin–orbit coupling via proximity to substrates, rotational symmetry in the spin space is broken. In such cases, we need to explore more spin configurations (including noncollinear ones) to obtain true ground states, which can be exotic.

Before closing, we would like to emphasize again that the nanoribbons with desired edge decoration have been synthesized [27] at least

without ports. Not necessarily limited to this specific type of decoration, recent progress in manipulation of graphene edge morphology is remarkable [38–47]. These developments encourage us to look for nanoscale spin devices realized by flake shape designs.

Declaration of competing interest

The authors declare the following financial interests/personal relationships which may be considered as potential competing interests: Toshikaze Kariyado reports financial support was provided by Japan Society for the Promotion of Science. If there are other authors, they declare that they have no known competing financial interests or personal relationships that could have appeared to influence the work reported in this paper.

Acknowledgments

This work was supported by JSPS KAKENHI, Japan Grant Number JP24K06968. The part of calculations in this study have been done using the Numerical Materials Simulator at NIMS, and the facilities of the Supercomputer Center, the Institute for Solid State Physics, the University of Tokyo.

Data availability

Data will be made available on request.

References

[1] S. Bandyopadhyay, B. Das, A.E. Miller, Supercomputing with spin-polarized single electrons in a quantum coupled architecture, Nanotechnology 5 (1994) 113–133, http://dx.doi.org/10.1088/0957-4484/5/2/007, URL https://iopscience.iop.org/article/10.1088/0957-4484/5/2/007.

[2] D. Loss, D.P. DiVincenzo, Quantum computation with quantum dots, Phys. Rev. A 57 (1998) 120–126, http://dx.doi.org/10.1103/PhysRevA.57.120, URL https://link.aps.org/doi/10.1103/PhysRevA.57.120.

[3] R. Hanson, D.D. Awschalom, Coherent manipulation of single spins in semiconductors, Nature 453 (2008) 1043–1049, http://dx.doi.org/10.1038/nature07129, URL https://www.nature.com/articles/nature07129.

[4] M. Veldhorst, C.H. Yang, J.C. Hwang, W. Huang, J.P. Dehollain, J.T. Muhonen, S. Simmons, A. Laucht, F.E. Hudson, K.M. Itoh, A. Morello, A.S. Dzurak, A two-qubit logic gate in silicon, Nature 526 (2015) 410–414, http://dx.doi.org/10.1038/nature15263.

[5] A.R. Rocha, V.M. García-Suárez, S.W. Bailey, C.J. Lambert, J. Ferrer, S. Sanvito, Towards molecular spintronics, Nat. Mater. 4 (2005) 335–339, http://dx.doi.org/10.1038/nmat1349.

[6] L. Bogani, W. Wernsdorfer, Molecular spintronics using single-molecule magnets, Nat. Mater. 7 (2008) 179–186, http://dx.doi.org/10.1038/nmat2133, URL https://www.nature.com/articles/nmat2133.

[7] S. Sanvito, Molecular spintronics, Chem. Soc. Rev. 40 (2011) 3336, http://dx.doi.org/10.1039/c1cs15047b, URL https://xlink.rsc.org/?DOI=c1cs15047b.

[8] S. Okada, A. Oshiyama, Magnetic ordering in hexagonally bonded sheets with first-row elements, Phys. Rev. Lett. 87 (2001) 146803, http://dx.doi.org/10.1103/PhysRevLett.87.146803, URL https://link.aps.org/doi/10.1103/PhysRevLett.87.146803.

[9] H. Lee, Y.-W. Son, N. Park, S. Han, J. Yu, Magnetic ordering at the edges of graphitic fragments: Magnetic tail interactions between the edge-localized states, Phys. Rev. B 72 (2005) 174431, http://dx.doi.org/10.1103/PhysRevB.72.174431, URL https://link.aps.org/doi/10.1103/PhysRevB.72.174431.

[10] O.V. Yazyev, M.I. Katsnelson, Magnetic correlations at graphene edges: Basis for novel spintronics devices, Phys. Rev. Lett. 100 (2008) 047209, http://dx.doi.org/10.1103/PhysRevLett.100.047209, URL https://link.aps.org/doi/10.1103/PhysRevLett.100.047209.

[11] O.V. Yazyev, Emergence of magnetism in graphene materials and nanostructures, Rep. Progr. Phys. 73 (5) (2010) 056501, http://dx.doi.org/10.1088/0034-4885/73/5/056501.

[12] J. Fernández-Rossier, J.J. Palacios, Magnetism in graphene nanoislands, Phys. Rev. Lett. 99 (2007) 177204, http://dx.doi.org/10.1103/PhysRevLett.99.177204, URL https://link.aps.org/doi/10.1103/PhysRevLett.99.177204.

[13] M. Ezawa, Metallic graphene nanodisks: Electronic and magnetic properties, Phys. Rev. B 76 (2007) 245415, http://dx.doi.org/10.1103/PhysRevB.76.245415, URL https://link.aps.org/doi/10.1103/PhysRevB.76.245415.

[14] W.L. Wang, S. Meng, E. Kaxiras, Graphene nanoflakes with large spin, Nano Lett. 8 (1) (2008) 241–245, http://dx.doi.org/10.1021/nl072548a.

[15] S. Bhowmick, V.B. Shenoy, Edge state magnetism of single layer graphene nanostructures, J. Chem. Phys. 128 (24) (2008) 244717, http://dx.doi.org/10.1063/1.2943678.

[16] D.P. Kosimov, A.A. Dzhurakhalov, F.M. Peeters, Carbon clusters: From ring structures to nanographene, Phys. Rev. B 81 (2010) 195414, http://dx.doi.org/10.1103/PhysRevB.81.195414, URL https://link.aps.org/doi/10.1103/PhysRevB.81.195414.

[17] W.L. Wang, O.V. Yazyev, S. Meng, E. Kaxiras, Topological frustration in graphene nanoflakes: Magnetic order and spin logic devices, Phys. Rev. Lett. 102 (2009) 157201, http://dx.doi.org/10.1103/PhysRevLett.102.157201, URL https://link.aps.org/doi/10.1103/PhysRevLett.102.157201.

[18] Z. Bullard, E.C. Girão, J.R. Owens, W.A. Shelton, V. Meunier, Improved all-carbon spintronic device design, Sci. Rep. 5 (1) (2015) 7634, http://dx.doi.org/10.1038/srep07634.

[19] L. Brey, H.A. Fertig, S. Das Sarma, Diluted graphene antiferromagnet, Phys. Rev. Lett. 99 (2007) 116802, http://dx.doi.org/10.1103/PhysRevLett.99.116802, URL https://link.aps.org/doi/10.1103/PhysRevLett.99.116802.

[20] N. Morishita, Y. Oishi, T. Yamaguchi, K. Kusakabe, S = 1 antiferromagnetic electron-spin systems on hydrogenated phenalenyl-tessellation molecules for material-based quantum-computation resources, Appl. Phys. Express 14 (12) (2021) 121005, http://dx.doi.org/10.35848/1882-0786/ac3b9d.

[21] G.Z. Magda, X. Jin, I. Hagymási, P. Vancsó, Z. Osváth, P. Nemes-Incze, C. Hwang, L. Biró, L. Tapasztó, Room-temperature magnetic order on zigzag edges of narrow graphene nanoribbons, Nature 514 (7524) (2014) 608–611, http://dx.doi.org/10.1038/nature13831.

[22] K. Nakada, M. Fujita, G. Dresselhaus, M.S. Dresselhaus, Edge state in graphene ribbons: Nanometer size effect and edge shape dependence, Phys. Rev. B 54 (1996) 17954–17961, http://dx.doi.org/10.1103/PhysRevB.54.17954, URL https://link.aps.org/doi/10.1103/PhysRevB.54.17954.

[23] K. Wakabayashi, S. Okada, R. Tomita, S. Fujimoto, Y. Natsume, Edge states and flat bands of graphene nanoribbons with edge modification, J. Phys. Soc. Japan 79 (3) (2010) 034706, http://dx.doi.org/10.1143/JPSJ.79.034706.

[24] D.J. Klein, L. Bytautas, Graphitic edges and unpaired π-electron spins, J. Phys. Chem. A 103 (26) (1999) 5196–5210, http://dx.doi.org/10.1021/jp990510j.

[25] D.J. Klein, T. Goswami, Y.P. Ortiz, Translationally symmetric graphene strips, J. Math. Chem. 58 (5) (2020) 1014–1024, http://dx.doi.org/10.1007/s10910-020-01112-7.

[26] M. Fujita, K. Wakabayashi, K. Nakada, K. Kusakabe, Peculiar localized state at zigzag graphite edge, J. Phys. Soc. Japan 65 (7) (1996) 1920–1923, http://dx.doi.org/10.1143/JPSJ.65.1920.

[27] A. Narita, X. Feng, Y. Hernandez, S.A. Jensen, M. Bonn, H. Yang, I.A. Verzhbitskiy, C. Casiraghi, M.R. Hansen, A.H.R. Koch, G. Fytas, O. Ivasenko, B. Li, K.S. Mali, T. Balandina, S. Mahesh, S. De Feyter, K. Müllen, Synthesis of structurally well-defined and liquid-phase-processable graphene nanoribbons, Nat. Chem. 6 (2) (2014) 126–132, http://dx.doi.org/10.1038/nchem.1819.

[28] R. Konnerth, C. Cervetti, A. Narita, X. Feng, K. MÃijllen, A. Hoyer, M. Burghard, K. Kern, M. Dressel, L. Bogani, Tuning the deposition of molecular graphene nanoribbons by surface functionalization, Nanoscale 7 (2015) 12807–12811, http://dx.doi.org/10.1039/C4NR07378A.

[29] A. Narita, Z. Chen, Q. Chen, K. Müllen, Solution and on-surface synthesis of structurally defined graphene nanoribbons as a new family of semiconductors, Chem. Sci. 10 (2019) 964–975, http://dx.doi.org/10.1039/C8SC03780A.

[30] T. Kariyado, X. Hu, Topological states characterized by mirror winding numbers in graphene with bond modulation, Sci. Rep. 7 (1) (2017) 16515, http://dx.doi.org/10.1038/s41598-017-16334-0.

[31] S.E. Freeney, J.J. van den Broeke, A.J.J. Harsveld van der Veen, I. Swart, C. Morais Smith, Edge-dependent topology in kekulé lattices, Phys. Rev. Lett. 124 (2020) 236404, http://dx.doi.org/10.1103/PhysRevLett.124.236404, URL https://link.aps.org/doi/10.1103/PhysRevLett.124.236404.

[32] http://www.openmx-square.org, accessed on the submission date. link. URL https://www.openmx-square.org.

[33] T. Ozaki, Variationally optimized atomic orbitals for large-scale electronic structures, Phys. Rev. B 67 (2003) 155108, http://dx.doi.org/10.1103/PhysRevB.67.155108, URL https://link.aps.org/doi/10.1103/PhysRevB.67.155108.

[34] T. Ozaki, H. Kino, Numerical atomic basis orbitals from H to Kr, Phys. Rev. B 69 (2004) 195113, http://dx.doi.org/10.1103/PhysRevB.69.195113, URL https://link.aps.org/doi/10.1103/PhysRevB.69.195113.

[35] T. Ozaki, H. Kino, Efficient projector expansion for the ab initio LCAO method, Phys. Rev. B 72 (2005) 045121, http://dx.doi.org/10.1103/PhysRevB.72.045121, URL https://link.aps.org/doi/10.1103/PhysRevB.72.045121.

[36] J.P. Perdew, K. Burke, M. Ernzerhof, Generalized gradient approximation made simple, Phys. Rev. Lett. 77 (1996) 3865–3868, http://dx.doi.org/10.1103/PhysRevLett.77.3865, URL https://link.aps.org/doi/10.1103/PhysRevLett.77.3865.

[37] E.H. Lieb, Two theorems on the Hubbard model, Phys. Rev. Lett. 62 (1989) 1201–1204, http://dx.doi.org/10.1103/PhysRevLett.62.1201, URL https://link.aps.org/doi/10.1103/PhysRevLett.62.1201.

[38] J. Cai, P. Ruffieux, R. Jaafar, M. Bieri, T. Braun, S. Blankenburg, M. Muoth, A.P. Seitsonen, M. Saleh, X. Feng, K. Müllen, R. Fasel, Atomically precise bottom-up fabrication of graphene nanoribbons, Nature 466 (7305) (2010) 470–473, http://dx.doi.org/10.1038/nature09211.

[39] G.D. Nguyen, H.-Z. Tsai, A.A. Omrani, T. Marangoni, M. Wu, D.J. Rizzo, G.F. Rodgers, R.R. Cloke, R.A. Durr, Y. Sakai, F. Liou, A.S. Aikawa, J.R. Chelikowsky, S.G. Louie, F.R. Fischer, M.F. Crommie, Atomically precise graphene nanoribbon heterojunctions from a single molecular precursor, Nature Nanotechnology 12 (11) (2017) 1077–1082, http://dx.doi.org/10.1038/nnano.2017.155.

[40] O. Gröning, S. Wang, X. Yao, C.A. Pignedoli, G. Borin Barin, C. Daniels, A. Cupo, V. Meunier, X. Feng, A. Narita, K. Müllen, P. Ruffieux, R. Fasel, Engineering of robust topological quantum phases in graphene nanoribbons, Nature 560 (7717) (2018) 209–213, http://dx.doi.org/10.1038/s41586-018-0375-9.

[41] M. Shekhirev, P. Zahl, A. Sinitskii, Phenyl functionalization of atomically precise graphene nanoribbons for engineering inter-ribbon interactions and graphene nanopores, ACS Nano 12 (8) (2018) 8662–8669, http://dx.doi.org/10.1021/acsnano.8b04489.

[42] C. Backes, A.M. Abdelkader, C. Alonso, A. Andrieux-Ledier, R. Arenal, J. Azpeitia, N. Balakrishnan, L. Banszerus, J. Barjon, R. Bartali, S. Bellani, C. Berger, R. Berger, M.M.B. Ortega, C. Bernard, P.H. Beton, A. Beyer, A. Bianco, P. Bøggild, F. Bonaccorso, G.B. Barin, C. Botas, R.A. Bueno, D. Carriazo, A. Castellanos-Gomez, M. Christian, A. Ciesielski, T. Ciuk, M.T. Cole, J. Coleman, C. Coletti, L. Crema, H. Cun, D. Dasler, D. De Fazio, N. Díez, S. Drieschner, G.S. Duesberg, R. Fasel, X. Feng, A. Fina, S. Forti, C. Galiotis, G. Garberoglio, J.M. García, J.A. Garrido, M. Gibertini, A. Gölzhäuser, J. Gómez, T. Greber, F. Hauke, A. Hemmi, I. Hernandez-Rodriguez, A. Hirsch, S.A. Hodge, Y. Huttel, P.U. Jepsen, I. Jimenez, U. Kaiser, T. Kaplas, H. Kim, A. Kis, K. Papagelis, K. Kostarelos, A. Krajewska, K. Lee, C. Li, H. Lipsanen, A. Liscio, M.R. Lohe, A. Loiseau, L. Lombardi, M. Francisca López, O. Martin, C. Martín, L. Martínez, J.A. Martin-Gago, J. Ignacio Martínez, N. Marzari, Á. Mayoral, J. McManus, M. Melucci, J. Méndez, C. Merino, P. Merino, A.P. Meyer, E. Miniussi, V. Miseikis, N. Mishra, V. Morandi, C. Munuera, R. Muñoz, H. Nolan, L. Ortolani, A.K. Ott, I. Palacio, V. Palermo, J. Parthenios, I. Pasternak, A. Patane, M. Prato, H. Prevost, V. Prudkovskiy, N. Pugno, T. Rojo, A. Rossi, P. Ruffieux, P. Samorì, L. Schué, E. Setijadi, T. Seyller, G. Speranza, C. Stampfer, I. Stenger, W. Strupinski, Y. Svirko, S. Taioli, K.B.K. Teo, M. Testi, F. Tomarchio, M. Tortello, E. Treossi, A. Turchanin, E. Vazquez, E. Villaro, P.R. Whelan, Z. Xia, R. Yakimova, S. Yang, G.R. Yazdi, C. Yim, D. Yoon, X. Zhang, X. Zhuang, L. Colombo, A.C. Ferrari, M. Garcia-Hernandez, Production and processing of graphene and related materials, 2D Mater. 7 (2) (2020) 022001, http://dx.doi.org/10.1088/2053-1583/ab1e0a.

[43] M. Pizzochero, G.B. Barin, K. Čerņevičs, S. Wang, P. Ruffieux, R. Fasel, O.V. Yazyev, Edge disorder in bottom-up zigzag graphene nanoribbons: Implications for magnetism and quantum electronic transport, J. Phys. Chem. Lett. 12 (19) (2021) 4692–4696, http://dx.doi.org/10.1021/acs.jpclett.1c00921, pMID: 33979153. arXiv:https://doi.org/10.1021/acs.jpclett.1c00921.

[44] R.S.K. Houtsma, J. de la Rie, M. Stöhr, Atomically precise graphene nanoribbons: interplay of structural and electronic properties, Chem. Soc. Rev. 50 (2021) 6541–6568, http://dx.doi.org/10.1039/D0CS01541E.

[45] D.J. Rizzo, J. Jiang, D. Joshi, G. Veber, C. Bronner, R.A. Durr, P.H. Jacobse, T. Cao, A. Kalayjian, H. Rodriguez, P. Butler, T. Chen, S.G. Louie, F.R. Fischer, M.F. Crommie, Rationally designed topological quantum dots in bottom-up graphene nanoribbons, ACS Nano 15 (12) (2021) 20633–20642, http://dx.doi.org/10.1021/acsnano.1c09503, pMID: 34842409. arXiv:https://doi.org/10.1021/acsnano.1c09503.

[46] A. Kinikar, X. Xu, M.D. Giovannantonio, O. Gröning, K. Eimre, C.A. Pignedoli, K. Müllen, A. Narita, P. Ruffieux, R. Fasel, On-surface synthesis of edge-extended zigzag graphene nanoribbons, Adv. Mater. 35 (48) (2023) 2306311, http://dx.doi.org/10.1002/adma.202306311, arXiv:https://advanced.onlinelibrary.wiley.com/doi/pdf/10.1002/adma.202306311. URL https://advanced.onlinelibrary.wiley.com/doi/abs/10.1002/adma.202306311.

[47] X. Zhu, K. Li, J. Liu, Z. Wang, Z. Ding, Y. Su, B. Yang, K. Yan, G. Li, P. Yu, Topological structure realized in cove-edged graphene nanoribbons via incorporation of periodic pentagon rings, J. Am. Chem. Soc. 146 (11) (2024) 7152–7158, http://dx.doi.org/10.1021/jacs.4c00270, pMID: 38421279. arXiv:https://doi.org/10.1021/jacs.4c00270.